RMetS
Royal Meteorological Society

Role of moisture patterns in the backbuilding formation of HyMeX IOP13 heavy precipitation systems

F. Duffourg,[a]* K.-O. Lee,[b] V. Ducrocq,[a] C. Flamant,[b] P. Chazette[c] and P. Di Girolamo[d]
[a]*CNRM, UMR3589, Météo-France & CNRS, Toulouse Cedex 1, France*
[b]*LATMOS/IPSL, UMR 8190, UPMC Université Paris 6, Sorbonne Universités, CNRS & UVSQ, Paris, France*
[c]*LSCE/IPSL, UMR 8212, CEA-CNRS-UVSQ, Gif-sur-Yvette, France*
[d]*Scuola di Ingegneria, Università degli Studi della Basilicata, Potenza, Italy*

*Correspondence to: F. Duffourg, CNRM, Météo-France, 42 avenue Gaspard Coriolis, 31057 Toulouse cedex 1, France.
E-mail: fanny.duffourg@meteo.fr

Mediterranean regions are regularly affected by heavy convective precipitation. During the Hydrological Cycle in the Mediterranean Experiment Intensive Observation Period 13 (HyMeX-IOP13), the multi-platform observation strategy allowed analysis of the backbuilding convective systems that developed on 14 October 2012, as well as the associated moisture structures in the environment upstream of convection.

The numerical simulation at 2.5 km horizontal resolution succeeds in reproducing the location and time evolution of the observed heavy precipitation systems and the main characteristics of the marine air mass. Convection develops in Southeastern France over the foothills closest to the coast when a moist conditionally unstable marine boundary layer topped by particularly dry air masses is advected inland. Cold air formed by evaporative cooling under the precipitating cells flows down the valleys, slowly shifting the location of the backbuilding convective cells from the mountainsides to the coast and over the sea. Surface observations confirm that these simulated backbuilding mechanisms describe the processes involved in maintenance of the heavy precipitation event realistically.

A Lagrangian analysis shows that the moisture supply to the convective system is provided by the moist conditionally unstable marine boundary layer, while the dry air masses above are involved in cold-pool formation. Four days before the event, both dry and moist air masses come from the Atlantic Ocean in the lower half of the troposphere. The dry air mass involved in cold-pool formation results from both the advection of mid-level air masses and the drying of low-level air masses lifted up over Spain. For the moist air mass feeding the backbuilding convective systems, most of the air parcels overpass France before travelling almost 48 h in the lowest 1000 m above the Mediterranean. About 50% of the moisture supply to the precipitating system originates from evaporation over the sea.

Key Words: heavy precipitation event; HyMeX; mesoscale convective system; field campaign observations; moisture structures

Received 2 January 2017; Revised 24 October 2017; Accepted 5 November 2017; Published online in Wiley Online Library 9 January 2018

1. Introduction

Heavy precipitation is a frequent and high-impact weather hazard affecting the Mediterranean regions (Ricard *et al.*, 2012; Llasat *et al.*, 2013). Large rainfall amounts can accumulate rapidly, typically more than 150 mm in less than 12 h. Such rainfall accumulations often cause flash floods with large material damages and human losses. These high-impact events are most often due to quasi-stationary mesoscale convective systems (MCSs: Romero *et al.*, 2000; Nuissier *et al.*, 2008; Buzzi *et al.*, 2014). Large rainfall amounts are obtained when a backbuilding MCS repeatedly renews convective cells upstream while older cells move downstream over the same region (Schumacher and Johnson, 2005; Ducrocq *et al.*, 2008).

Past studies have investigated the synoptic patterns favouring such high-impact events (Rudari *et al.*, 2004; Martínez *et al.*, 2008; Nuissier *et al.*, 2008, 2011). Over the Western Mediterranean region, MCSs develop preferentially eastward of a slow-evolving disturbance associated with an upper-level trough extending over the Iberian Peninsula and leading a southwesterly diffluent flow at high altitude. Such a synoptic pattern favours a persistent low-level moist and conditionally unstable marine flow directed towards the coastal mountainous regions.

Different lifting mechanisms enabling the release of conditional convective instability have been identified (Ducrocq *et al.*, 2008). Orographic lifting of the conditionally unstable low-level marine flow impinging upon the foothills bordering the western Mediterranean is a well-known mechanism for renewing convection triggering at the same location (Barthlott and Davolio, 2016). Lifting can also be due to local convergence in the low-level circulation induced by the orography of the region (Barthlott *et al.*, 2016; Buzzi *et al.*, 2014; Scheffknecht *et al.*, 2016) or lee cyclogeneses (Duffourg *et al.*, 2016). A low-level cold pool, possibly formed under the MCS, can also lift the low-level flow at its leading edge (Ducrocq *et al.*, 2008) or modify the low-level circulation locally and enhance convergence areas (Duffourg *et al.*, 2016). Idealized studies have shown that the lifting mechanisms and consequently the location and intensity of the precipitating convective systems are sensitive to the characteristics of the upstream flow and the environment (Miglietta and Rotunno, 2010; Bresson *et al.*, 2012; Davolio *et al.*, 2016). For example, the formation of a cold pool has been shown to occur when the ambient flow is relatively dry or weak (Bresson *et al.*, 2012). However, the sensitivity of convective mechanisms to the characteristics of the environment has not been studied much in real heavy precipitation events (HPEs) yet. In particular, the impact of surrounding dry air masses on the development and evolution of MCSs is still unclear.

On 14 October 2012, during Intensive Observation Period 13 (IOP13) of the first Special Observation Period (SOP1) of the Hydrological Cycle in the Mediterranean Experiment (HyMeX), backbuilding heavy precipitation convective systems developed in an environment with a dry layer on top of the about 1200 m deep moist conditionally unstable boundary layer and extremely dry air around 2500 m above sea level (ASL). The instruments deployed during SOP1 (Ducrocq *et al.*, 2014) observed these moisture structures and the convective systems. Taking benefit from the large and unique dataset collected during SOP1, the present article aims to analyse the moisture structures of the environment and their impact on the convective mechanisms involved in the development and maintenance of the backbuilding MCS.

The characteristics of the moisture patterns of the environment are firstly analysed thanks to the HyMeX observations. The convective systems and their environment are then reproduced in a numerical simulation of the HPE. The simulated convective mechanisms are examined and a numerical analysis of the origin, formation and impact of the moisture structures on the convective mechanisms is conducted. The outline of the article is as follows. The precipitating event and the associated synoptic pattern are presented in section 2, together with the available HyMeX observations. Section 3 describes the numerical set-up and evaluates the quality of the simulated convective systems. Section 4 details the moisture and wind characteristics of the environment, before investigating the convective mechanisms for the initiation and maintenance of the IOP13 precipitating systems. Section 5 examines the origin of the moisture structures involved in the convective mechanisms identified. Conclusions are given in section 6.

2. IOP13 overview

2.1. Description of the precipitation event

Around midday on 14 October 2012, isolated convective cells were initiated offshore, a few kilometres southwest of the Var region and southwest of Marseille (the position of these geographical areas is given in Figure 1). They developed over land and rapidly organized into two backbuilding convective systems (Figure 1) in the surroundings of Marseille (MCS1) and over the Var region (MCS2). MCS1 had strong activity from about 1330 UTC until 1430 UTC, with a tornado observed north of Marseille at 1340 UTC. After a period of more disorganized and weaker convective activity over the mountainous area north of Marseille, the system organized into a strong backbuilding convective line

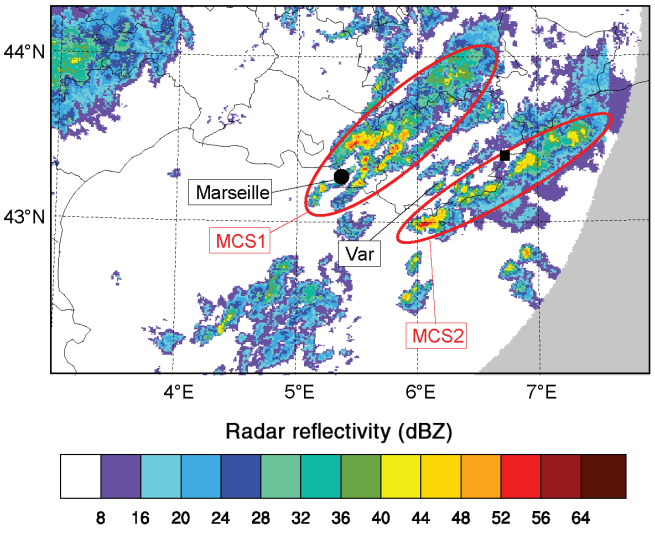

Figure 1. Composite image of radar reflectivities (dBZ) measured at 1800 UTC on 14 October 2012. The black square shows the location of Fréjus, where the maximum 6 h rainfall accumulation was recorded by a rain-gauge.

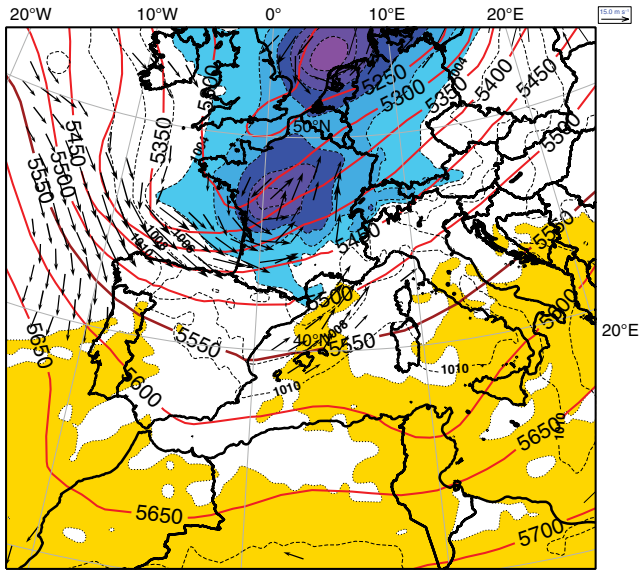

Figure 2. ARPEGE analysis at 1200 UTC on 14 October 2012 of the geopotential height at 500 hPa (m, thick red isolines every 50 m), mean sea-level pressure (hPa, dashed isolines every 2 hPa and colour scale under 1006 hPa), wet-bulb potential temperature (yellow area with dotted isolines above 15 ° C) and horizontal wind (arrows for wind speed above 15 m s^{-1} at 925 hPa. The region displayed in this figure matches the domain of the ARP10 simulation. [Colour figure can be viewed at wileyonlinelibrary.com].

and remained quasi-stationary from about 1630–1800 UTC, before shifting eastwards and dissipating slowly over the Var region after 1900 UTC. The maximum rainfall accumulation related to this system was recorded near Aix-en-Provence, 25 km north of Marseille, with up to 80 mm in 6 h. MCS2 developed into a stationary convective line along the eastern Var coast around 1400 UTC. It remained quasi-stationary over the same area all afternoon, before moving eastwards after 1900 UTC. Radar quantitative precipitation estimates (not shown) indicate that up to 170 mm of precipitation in 12 h were observed a few kilometres offshore of the Var coast and 67 mm were recorded in the same time by a coastal rain-gauge (Fréjus: 6.74° E, 43.42° N).

2.2. Synoptic context

The synoptic situation on 14 October 2012 is summarized in Figure 2. It is characterized by an upper-level trough associated with a surface low situated over northwestern France at 1200 UTC. Ahead of its cold front, a southwesterly low-level flow over

the Mediterranean French coast brings a warm marine air mass inland. The mean sea-level pressure along the Spanish coast on the Balearic Sea is perturbed by a secondary cyclonic wave at 1200 UTC (see Figure 2). At higher levels over this area, the flow is westsouthwesterly and slightly divergent. The vertical shear of the horizontal wind above the boundary layer is almost unidirectional. This synoptic pattern slowly shifted southeastwards during the day.

2.3. *HyMeX observations*

During HyMeX SOP1, more than 200 research instruments were deployed over the northwestern Mediterranean Sea and its surrounding coastal regions in France, Italy and Spain. They ensured observation of the precipitating systems and provided dense measurements of the upstream meteorological conditions over the sea. The observational means deployed are described comprehensively in Ducrocq *et al.* (2014). Among them, several wind profilers were deployed along the northwestern Mediterranean coast, including a UHF profiler in Ile du Levant (see Figure 3 for location). It provides valuable information on the vertical wind profile in the lower half of the troposphere just upstream of the Var region at 55 levels every 4 min (Saïd *et al.*, 2016). The Water Vapour and Aerosol Lidar (WALI: Chazette *et al.*, 2014) was operated in Ciutadella (Menorca, Balearic Islands; see Figure 3 for location) and the water vapour and temperature Raman lidar system (BASIL: Di Girolamo *et al.*, 2009) in Candillargues (see Figure 3 for location).

Many campaign observation systems were operated on alert. For IOP13, additional radiosoundings were launched in Marseille (see Figure 3 for location) every 3 h from 0900 UTC on 14 October. Also, the upstream low-level flow was sampled by the water-vapour lidar Lidar Embarqué pour l'étude des Aérosols, Nuages, Dynamique, Rayonnement et Espèces minoritaires (LEANDRE2) (Bruneau *et al.*, 2001) flown on board the ATR42 aircraft from the Service des Avions Français Instrumentés pour la Recherche en Environnement (SAFIRE), operating between Candillargues and Menorca during the morning and early afternoon of 14 October. The flight track and timing are displayed in Figure 3. Also, two boundary-layer pressurized balloons (Doerenbecher *et al.*, 2013) were launched from Menorca at 0610 and 0820 UTC on 14 October. They followed the southwesterly flow at a height of about 925 and 950 hPa respectively.

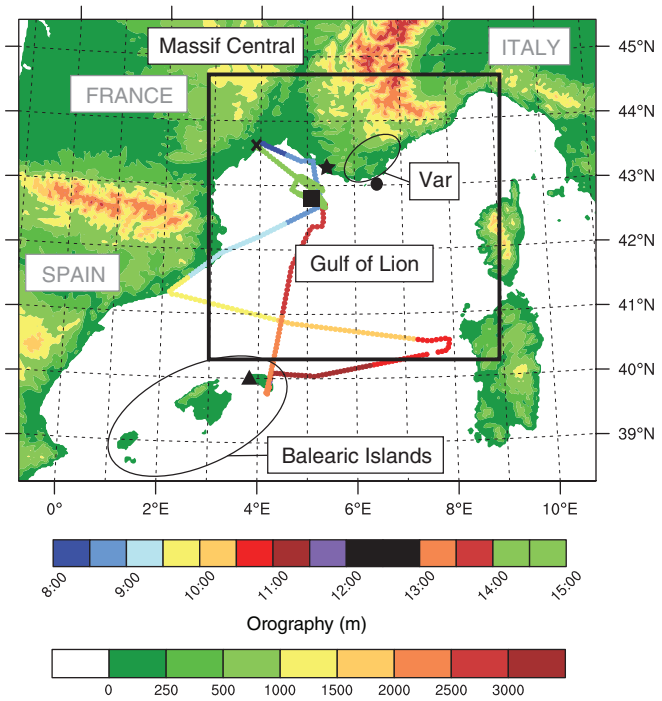

Figure 3. Domain of AW2.5 simulation (solid black rectangle) and orography (colour scale on the right, m). The timing of the flight track of the ATR42 aircraft is indicated by coloured dots (colour bar at the bottom). The names of the main geographical areas are also given. The black star is located in Marseille, the black circle at Ile du Levant, the black cross in Candillargues and the black triangle in Ciutadella (Menorca). The black square shows the area where the ATR aircraft performed a sounding.

3. Numerical simulation

3.1. *Meso-NH model configuration*

The HPE of IOP13 was simulated using the French non-hydrostatic numerical research model Meso-NH (Lafore *et al.*, 1998). For a fine-scale analysis of the precipitating systems and their short-range interactions with the environmental moisture structures, a 2.5 km horizontal resolution simulation, referred to below as AW2.5, was performed. The set-up is the same as in Duffourg *et al.* (2016), where it was able to reproduce convective systems realistically. It includes the same simulation domain over southeastern France and the northwestern Mediterranean (see Figure 3, $500 \times 500\,\mathrm{km}^2$ domain encompassing the precipitating systems and their marine low-level moisture-supplying flow), the same vertical grid with 55 stretched vertical levels (Gal-Chen and Somerville, 1975) up to 20 km and the same parametrization schemes: the bulk one-moment mixed microphysical scheme (Caniaux *et al.*, 1994; Pinty and Jabouille, 1998) combining a three-class ice parametrization with a Kessler's scheme for the warm processes, the Rapid Radiation Transfer Model parametrization (Mlawer *et al.*, 1997), the one-dimensional turbulence parametrization based on a 1.5-order closure (Cuxart *et al.*, 2000) of the Turbulent Kinetic Energy (TKE) equation with the Bougeault and Lacarrère (1989) mixing length, the Pergaud *et al.* (2009) Eddy Diffusivity Mass Flux scheme for shallow convection and the surface model SURFace EXternalisé (SURFEX) (Masson *et al.*, 2013). Only the transport scheme for momentum variables was changed to the computationally less expensive Weighted Essentially NonOscillatory (WENO) scheme (Shu and Osher, 1988), while other variables are still transported with the Piecewise Parabolic Method (PPM) scheme (Collela and Woodward, 1984). The simulation was initiated at 0600 UTC on 14 October 2012. As in Duffourg *et al.* (2016), the initial and lateral boundary conditions are provided by the AROME-WMED analyses (Fourrié *et al.*, 2015). AROME-WMED is a dedicated version of the French operational convection-permitting numerical prediction system Application of Research to Operations at MEsoscale (AROME: Seity *et al.*, 2011), set up specifically for the HyMeX campaign and covering the western Mediterranean. AROME-WMED was run with a three-hourly 3D-Var data assimilation cycle, at 2.5 km horizontal resolution. It assimilates all conventional routine observations (surface observations from land stations and ships, vertical soundings from radiosondes and pilot balloons, buoy and aircraft measurements), together with some wind profilers, winds from atmospheric motion vectors (AMV) and scatterometers, Doppler winds and reflectivities from radars, satellite radiances and ground-based Global Positioning System (GPS) measurements.

A 10 km horizontal resolution simulation, hereafter named ARP10, was also run in order to study the longer-range evolution of the moisture structures involved in the IOP13 HPE. The simulation domain, shown in Figure 2, covers the eastern part of the Atlantic Ocean as well as northern Africa. The same levels in the vertical and the same parametrizations and surface schemes as for AW2.5 are used, with an additional scheme for deep convection based on Kain and Fritsch (1993). ARP10 was initialized 4 days before the HPE, at 0000 UTC on 10 October 2012. The initial and lateral boundary conditions are provided by the six-hourly analyses from ARPEGE (Courtier *et al.*, 1991), the French operational global numerical weather prediction model.

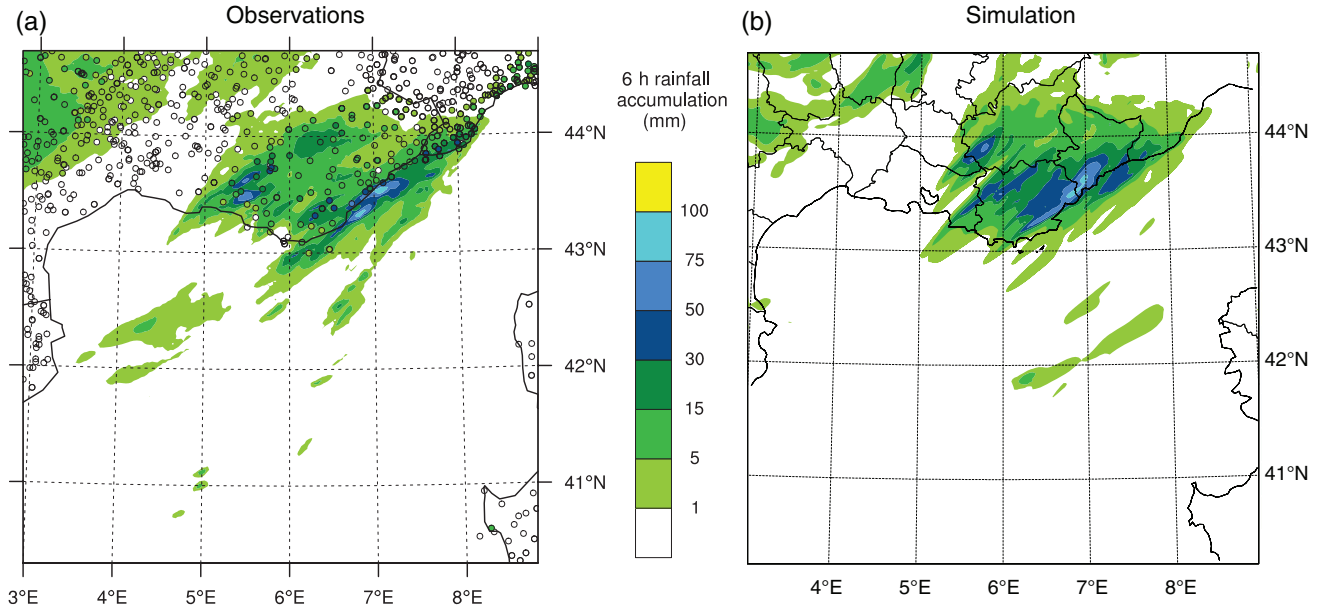

Figure 4. Six-hour rainfall accumulation (mm) (a) measured by the rain-gauges (coloured dots) and estimated from the French radar network (coloured areas) and (b) simulated by AW2.5 at 1800 UTC on 14 October 2012. [Colour figure can be viewed at wileyonlinelibrary.com].

3.2. Evaluation of the precipitating system simulated at 2.5 km horizontal resolution

As the precipitation occurred mainly during the afternoon, a comparison of the 6 h rainfall accumulation simulated by AW2.5 and observed between 1200 and 1800 UTC (Figure 4) provides a broad picture of the skill of the simulation. The simulated amount of rainfall accumulation is realistic, with more than 75 mm in 6 h associated with the convective line over the eastern Var coast (MCS2: 7° E) and slightly more than 50 mm for MCS1 near Marseille. The simulated precipitation due to MCS2 is well located, only about 10 km too far north, on the southernmost foothills rather than on the coast. The maximum of precipitation associated with MCS1 is not simulated near Aix-en-Provence but 30–40 km further inland to the northnortheast.

The radar reflectivities displayed in Figure 5 detail the time evolution of the precipitating systems simulated by AW2.5 and observed during the afternoon, at 1400, 1600 and 1800 UTC. The strength of MCS1 in the surroundings of Marseille is underestimated and it is located too far inland over the mountains by AW2.5. Over the Var region, the time evolution of the simulated convection matches the observations well. In the simulation, as in the observations, convection is initiated over the sea, a few kilometres offshore, around 1200 UTC (not shown) and is then advected inland northeastwards. It reaches the east of the Var region at 1430 UTC in the simulation, only 30 min later than observed (Figure 5(a)), and stays in this area (Figures 5(d)–(f)) until 1900 UTC, as in the observations (Figures 5(c)–(e)). In both the observations and the simulation, the convective line shifts southeastwards very slowly during the afternoon. However, the simulated convection strengthens and organizes earlier, as early as 1300 UTC, inducing too large a rainfall amount over the orography of Sainte-Baume (inland, west of the Var region; see Figure 9 for location). Also, the simulated convective line remains about 10 km too far inland and affects a slightly larger area.

In the following, the article will focus on the convective line over the Var region, the life cycle of which is well reproduced by AW2.5.

4. Environment and lifting mechanisms

4.1. Environment moisture and winds

To characterize the air mass supplying the precipitating system, backward trajectories of air parcels reaching the top of the simulated convective ascents are performed. The movement of the air parcels is computed as described in Gheusi and Stein (2002), using the technique developed by Schär and Wernli (1993). It is based on the on-line advection, along with the model dynamics at each model time step of the initial grid-point positions as Eulerian passive tracers. For analysis and plotting purposes, output with the positions of the air parcels is produced every 15 min. The horizontal projection of some of these backward trajectories for parcels at the top of the simulated convective ascents at 1600 UTC is superimposed on the radar reflectivities simulated by AW2.5 at 2000 m at 1600 UTC in Figure 6. It shows that convective ascents are fed by the southwesterly marine flow. This flow does not show any marked convergence. The vertical projection of backward trajectories (not shown) is evidence that the flow is confined to the lowest 1000 m above the sea surface before being lifted up to the top of the troposphere within 1 h in the convective ascents of the precipitating system. The low-level flow brings a moist (about 10 g kg^{-1}) and warm (θ_e about 322 K) air mass from east of Catalonia at 0800 UTC to the southeastern French coasts, where it feeds the convective ascents.

HyMeX observations provide quite a complete description of the characteristics of the environment in which the convective systems developed. Over the sea upstream of convection, the LEANDRE2 lidar observed the vertical structure of the water-vapour mixing ratio field along the flight track of the ATR42 aircraft (see Figure 3). Near the surface, the measurements are averaged over the lowest 400 m ASL to reduce the measurement-error variance. Figure 7 displays both a cross-flow leg between 0935 and 1035 UTC (yellow and orange tracks in Figure 3) and an along-flow leg between 1310 and 1357 UTC (light and dark pinkish-orange tracks in Figure 3). Comparing the ATR flight track (Figure 3) and the backward trajectories (Figure 6) showing the location over the sea of the low-level flow feeding convection, it appears that the ATR cross-flow leg intersects the southwesterly feeding flow almost perpendicularly. Its along-flow leg follows the feeding flow with a slightly more south–north trajectory. The ATR flight track and the backward trajectories do not coincide exactly in time, but the time shift is small (mostly about 1 h) and the simulated moisture content of the feeding flow over the Mediterranean does not change substantially in the morning.

Above the sea surface, LEANDRE2 measurements (Figure 7) show a well-mixed layer with large moisture content (about 11 g kg^{-1}). The moisture content measured is smaller (about 8 g kg^{-1}) in the eastern part of the cross-flow leg (see Figure 7(a) after 1020 UTC), as the ATR is too far to the east of the feeding flow

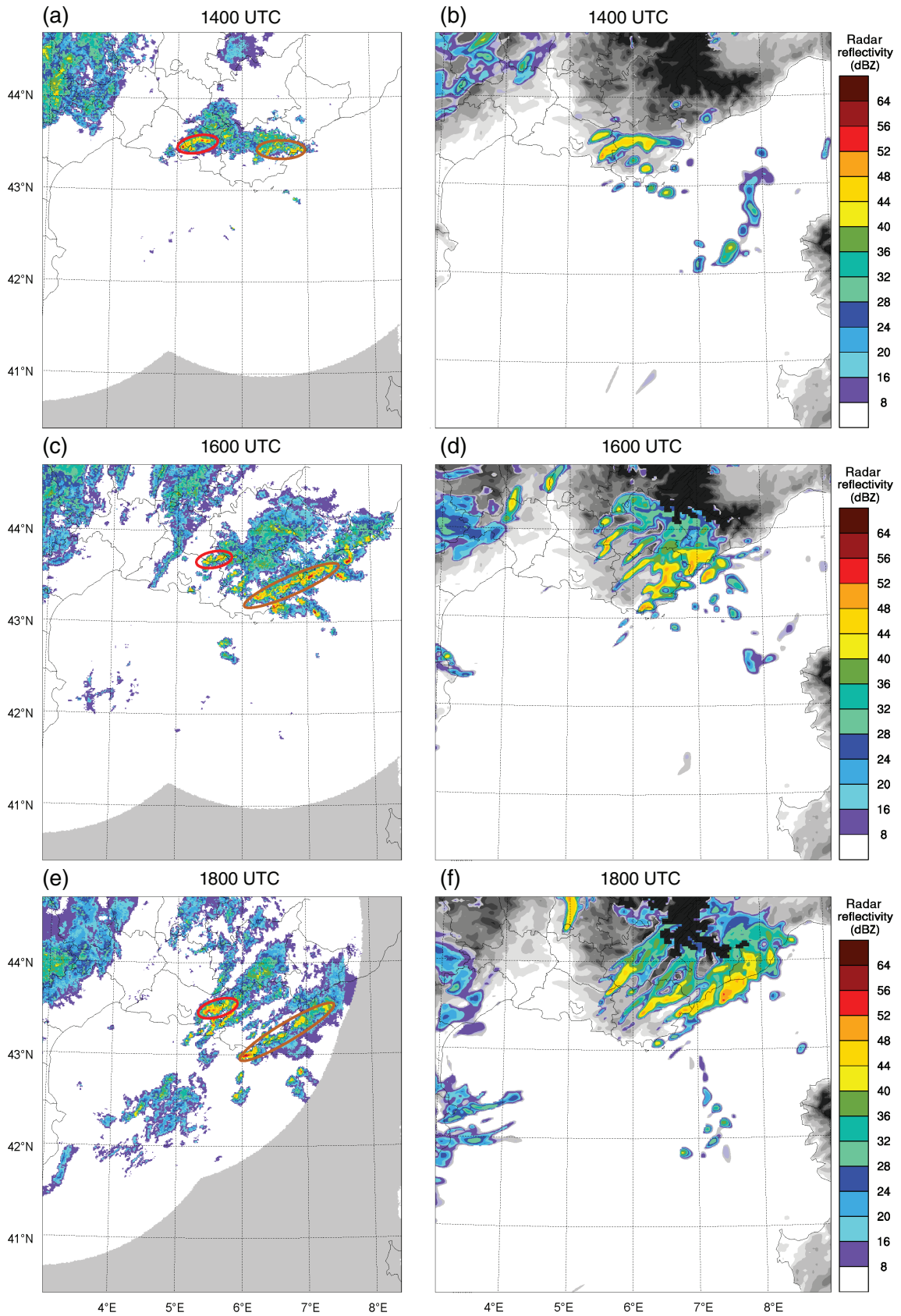

Figure 5. Radar reflectivities (dBZ) (a, c, e) measured and (b, d, f) simulated by AW2.5 at 2000 m at (a, b) 1400 UTC, (c, d) 1600 UTC and (e, f) 1800 UTC on 14 October 2012. The areas with no radar observation data are displayed in grey. MCS1 is circled in grey and MCS2 in brown.

evidenced by the backward trajectories. The mixed layer deepens slightly (by about 150 m) and moistens (by about 1 g kg^{-1}) between both legs. Its height also increases when the aircraft comes closer to the coastal convective area (in the northern part of the along-flow leg (Figure 7(b)) after 1330 UTC). Above the boundary layer, the moisture content decreases dramatically, with about 4–6 g kg^{-1} around 1500 m ASL and 1–3 g kg^{-1} above 2500 m ASL. Water-vapour mixing ratio measurements from BASIL indicated that this dry air mass observed with LEANDRE2 was also present over land since at least 2200 UTC on 13 October (Di Girolamo *et al.*, 2016). Also, a similar vertical structure of the moisture field with very dry air above a moist marine boundary layer was still observed 1 day later over the Tyrrhenian Sea, in association with heavy convective precipitation in the south of Italy (Lee *et al.*, 2016). The moisture content simulated with AW2.5 along the backward trajectories (about 10 g kg^{-1} below

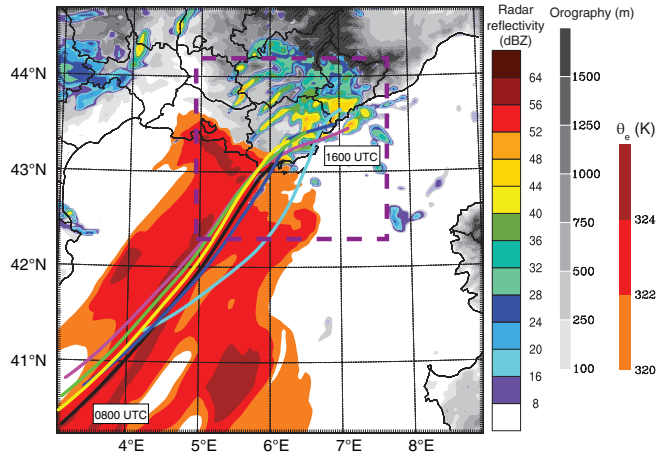

Figure 6. Horizontal projection of backward trajectories of some air parcels taken in the upper part of the convective line simulated by AW2.5 at 1600 UTC, together with radar reflectivities at 2000 m simulated at 1600 UTC by AW2.5 (coloured areas) and equivalent potential temperature θ_e at 925 hPa (K, red areas) simulated at 1400 UTC. The timing of the trajectories is indicated in UTC. The orography is displayed as a grey-scale. The dark magenta dashed rectangle shows the domain of the zoom used for Figure 9.

800 m ASL) and along the ATR flight legs (not shown) agrees well with the LEANDRE2 observations. However, the simulated well-mixed layer seems to be about 200 m too deep (mainly in the cross-flow leg) and the vertical gradient is less sharp in the simulation, as also observed in AROME-WMED analyses over the Balearic Sea during IOP 15a by Lee *et al.* (2017).

The vertical sounding (not shown) performed with the ATR aircraft around the position marked in Figure 3 (black square) evidences a similar vertical structure of the moisture field to that in LEANDRE2 measurements. The measured relative humidity up to 1200 m ASL is large, more than 85%. It decreases above, mainly between 2300 m and 3500 m ASL, with a relative humidity minimum down to 20% at 2500 m ASL.

The two pressurized balloons launched from Menorca that drifted in the southwesterly low-level flow at about 925 and 950 hPa, respectively, show a continuous increase of the wind speed as they approach the coast (not shown). The wind simulated by AW2.5 agrees well with the balloon observations for both direction and wind speed.

At the coast, the wind profiler installed during the HyMeX SOP1 on the Ile du Levant provides measurements of vertical profiles of horizontal winds immediately upstream of convection. They are displayed in Figure 8, together with the winds simulated by AW2.5. Near the surface, weak westerlies prevail in the morning. After 1200 UTC, the wind reinforces and turns more to the south (southsouthwesterly near the surface, southwesterly above 1000 m ASL). A wind-speed maximum characteristic of a low-level jet is observed between 1500 and 1800 UTC, just below 1000 m ASL (grey ellipsis in Figure 8). At the end of the HPE, the winds weaken and turn westsouthwest. The wind simulated by AW2.5 compares well with the observations in terms of both direction and wind speed until 1500 UTC. After this, it is too weak and the simulated low-level jet is oriented slightly too south.

The air mass over southeastern France becomes conditionally unstable between 1200 and 1500 UTC, according to both the radiosounding measurements in Marseille and the simulation. A comparison of the radiosounding at 1500 UTC with the vertical profiles of temperature, moisture and wind simulated in Marseille by AW2.5 shows that the thermodynamic characteristics of the marine air mass advected inland are quite well reproduced (not shown), in particular in the boundary layer and the dry layer near 2500 m ASL (water-vapour mixing ratio lower than 3 g kg^{-1}). The simulated Convective Available Potential Energy (CAPE) is about 1550 J kg^{-1}, while about 1600 J kg^{-1} was measured. However, the level of free convection (LFC) is too high, at 930 hPa instead of the observed 1000 hPa.

To sum up, the HyMeX observations show a marine moist southwesterly low-level jet feeding convection over the Var region, topped with a drier layer and extremely dry air above 2500 m ASL. The low-level flow and the moisture structures are well reproduced in the AW2.5 simulation.

4.2. *Initiation and continuous backbuilding mechanisms*

In the morning of 14 October 2012, the marine air mass simulated by AW2.5 south of the French coasts is conditionally unstable (CAPE of 1000–1500 J kg^{-1}) with a very low LFC (about 1000 hPa), resulting in almost no Convective INhibition (CIN). Within this conditionally unstable flow, the first convective cells form near shore shortly before midday, probably associated with local orography-induced wind convergence just upwind of the coastal mountains (the horizontal wind at 925 hPa is deflected slightly by the coastal orography at the southern tip of the Var region; not shown). Later, from 1300 UTC, more intense convection develops over the foothills closest to the coast.

Figure 9 displays the hourly evolution of the equivalent potential temperature θ_e at 925 hPa and the virtual potential temperature at the first model level (about 9 m high), together with the horizontal wind and the vertical velocity at 500 m ASL simulated by AW2.5 between 1400 and 1700 UTC. During the

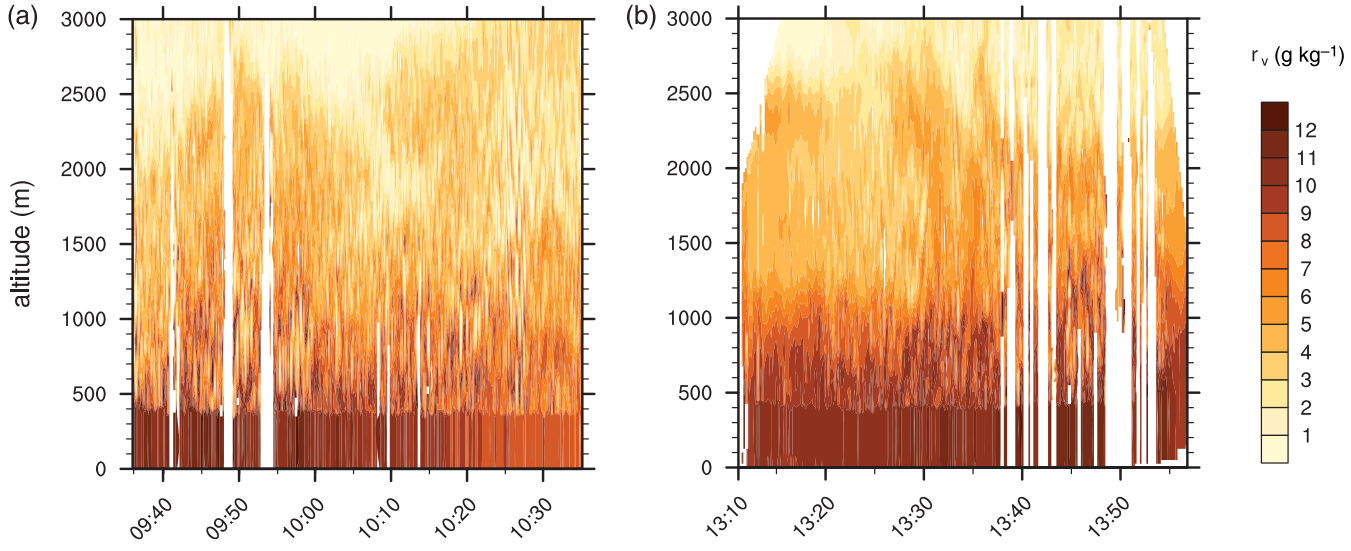

Figure 7. Water-vapour mixing ratio observed by LEANDRE2 during (a) a cross-flow leg and (b) an along-flow leg. [Colour figure can be viewed at wileyonlinelibrary.com].

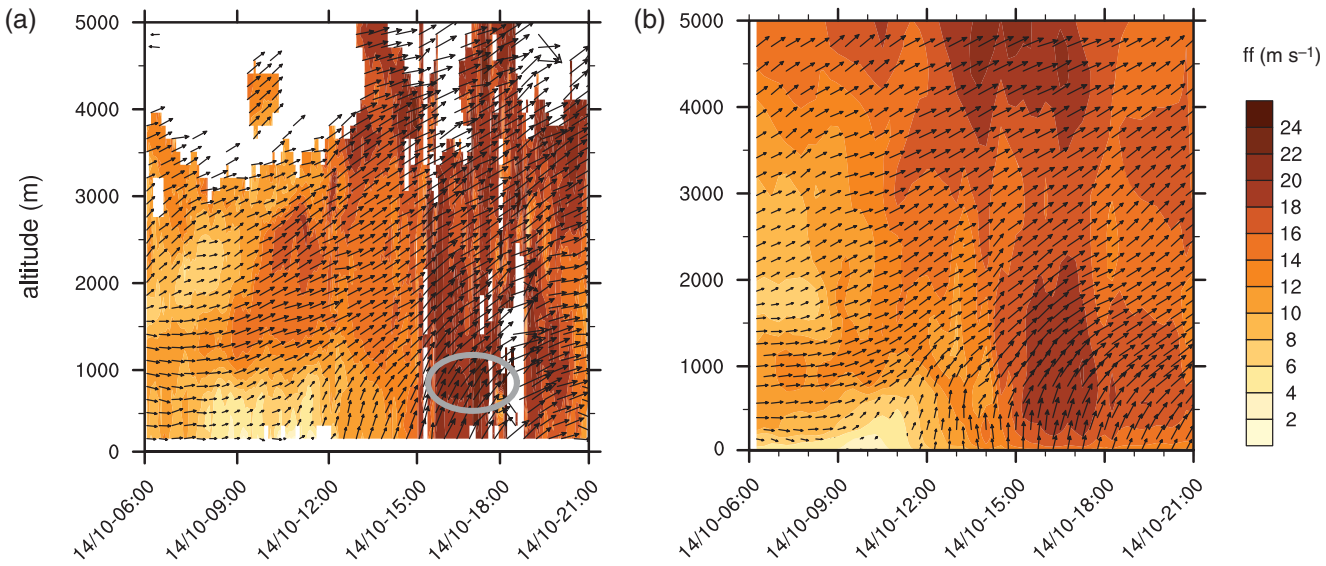

Figure 8. Horizontal wind (a) observed and (b) simulated by AW2.5 at the Levant wind profiler. The low-level jet is circled in grey. [Colour figure can be viewed at wileyonlinelibrary.com].

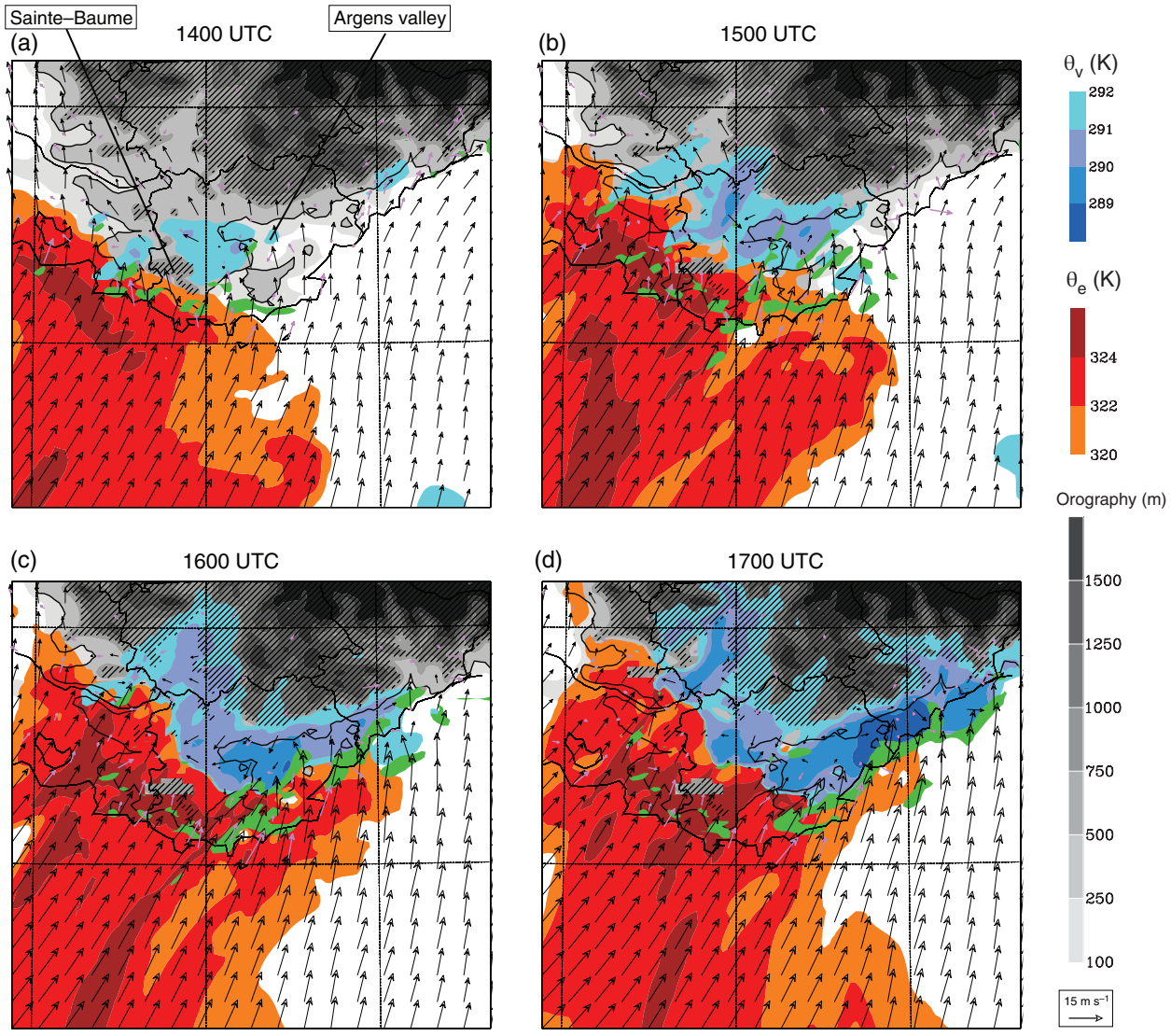

Figure 9. Equivalent potential temperature θ_e at 925 hPa (K, red areas), virtual potential temperature θ_v at the first model level (K, blue areas below 292 K), vertical wind speed at 500 m ASL (green areas above 0.5 m s^{-1}) and horizontal wind at 500 m ASL (m s^{-1}, arrows) simulated by AW2.5 for every hour between 1400 UTC and 1700 UTC and zoomed in to the domain displayed with dark magenta dashes in Figure 6. The orography (m) is in grey-scale form and the bold black line marks the 250 m terrain line. The thick pink arrows show the 10 m horizontal wind observed with the same scale as for the simulated 500 m horizontal wind.

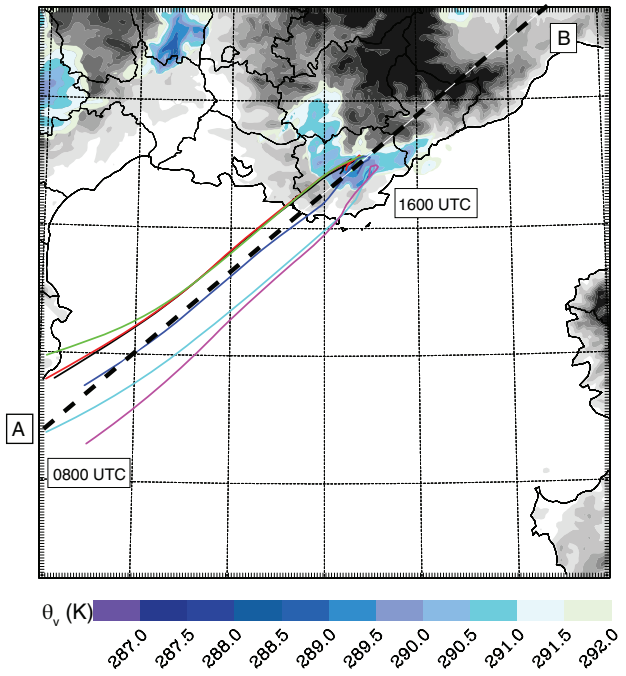

Figure 10. Horizontal projection of backward trajectories of some air parcels taken in the cold pool simulated by AW2.5 at 1600 UTC, together with the virtual potential temperature θ_v at the first model level (K, blue areas below 292 K). The timing of the trajectories is indicated in UTC. The orography is displayed with the same grey-scale as in Figure 9. The dashed line A–B shows the alignment of the vertical cross-section in Figure 11.

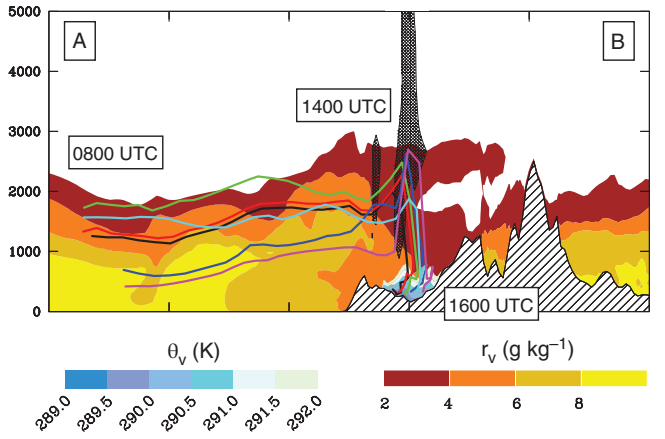

Figure 11. Vertical projection of backward trajectories of some air parcels taken in the cold pool under the convective line simulated by AW2.5 at 1600 UTC and vertical cross-section of water-vapour mixing ratio (colour scale, g kg^{-1}) simulated at 0800 UTC along the line A–B shown in Figure 10. The location of the system simulated at 1400 UTC is shown with dotted areas for hydrometeor content exceeding 1 g kg^{-1}. The area with θ_v below 292 K simulated at 1600 UTC is coloured in blue. The timing of the trajectories is indicated in UTC and the orography is hatched.

afternoon, the marine warm and moist low-level jet simulated by AW2.5 shifts progressively eastwards (Figure 9). It reaches the Var coast at 1600 UTC. Cold air ($\theta_v < 290$ K) forms by evaporative cooling under the precipitating cells and flows down the valleys, as evidenced from 1500 UTC by both the 500 m horizontal wind simulated by AW2.5 and the 10 m wind observed by the surface stations. It gradually fills up the Argens valley, blocking the inland advection of the marine moist low-level flow. After 1500 UTC, the main convective ascents are localized along coast on the mountainsides, but also on the leading edge of the cold air channelled in the Argens valley. During the entire afternoon, the lifting mechanism pattern remains similar, with even colder air in the Argens valley spreading out over the plains upstream of the coastal orography. The cold pool thus plays a major role in determining the location of the precipitation. It gradually shifts the main ascents from the bottom of the valleys to the coasts and over the sea.

A comparison of the simulation with wind and temperature surface observations shows that the simulated backbuilding mechanisms describe realistically the processes involved in the maintainance of this HPE. The formation of the cold pool in the Argens valley is also well simulated. The decrease of the simulated 2 m temperature is similar to the observations in both magnitude and timing (not shown). The simulated low-level wind is also consistent with the 10 m observations (Figure 9). Both show that the marine air mass enters the Argens valley at 1400 UTC, but the wind is reversed when the cold-air pool fills up the valley. Accordingly, the same shifting of the convective line from the bottom of the valley towards the coast upstream of the low-level marine flow appears in the simulation as in the observations (see Figures 5(a)–(d)), even if the simulated system remains more inland over a higher orography because of a higher LFC. This explains why the simulated precipitation is located slightly more inland.

Backward trajectories are also computed to identify the air mass involved in the formation of the cold-air pool channelled in the Argens valley. The backward trajectories computed from the core of the cold pool all follow a similar pathway. Some of these trajectories are selected to give an idea of the horizontal and vertical extension of this track. Their horizontal projection superimposed on the virtual potential temperature θ_v at the first model level simulated at 1600 UTC is displayed in Figure 10. Their vertical projection is presented in Figure 11, together with the virtual potential temperature θ_v simulated at 1600 UTC, the hydrometeor contents at 1400 UTC and the water-vapour mixing ratio simulated at 0800 UTC. Figure 11 shows that the air mass involved in cold-air pool formation comes mainly from a dry layer between 1000 and 2000 m ASL, just above the boundary layer, with water-vapour mixing ratios ranging between 6 and 3 g kg^{-1}. In the on-line computation of the backward trajectories, the air parcels are considered as passive tracers transported with the mean flow and subgrid turbulent motions. They thus undergo the mixing in the convective cloud. As shown by the evolution of the water-vapour mixing ratio of the air parcels along their trajectory, the air mass remains dry (about 5 g kg^{-1}) until it is entrained in the convective system at 1400 UTC. The water-vapour mixing ratio of the air parcels then increases rapidly up to 9 g kg^{-1} while they descend towards the surface. During the same time, their virtual potential temperature decreases from about 296 K before being entrained in the convective system to about 290 K in the cold pool. This confirms the formation process of the cold-air pool. The dry air mass is moistened and cooled down by the evaporation of part of the precipitation passing through. The moistened and cooled air mass is entrained by downdraughts, eventually forming a cold pool at the surface.

Some air parcels also come from the same height as the low-level flow supplying the convective system, but slightly more to the north. Because the directional vertical wind shear is weak, the trajectories within and above the boundary layer have the same direction (see Figure 10).

The ATR flight track (Figure 3) is slightly too far to the the south in comparison with the cold-pool air mass trajectories, as evidenced in Figure 10. However, LEANDRE2 still shows a drier layer around 1500 m ASL, with water-vapour mixing ratio ranging between 3 and 7 g kg^{-1}.

A Lagrangian analysis of the very dry layer above 2500 m ASL identified in the LEANDRE2 measurements and sounding observations was performed thanks to forward trajectories (not shown) at 1600 UTC of air parcels taken in this very dry area. The dry air parcels are advected in the surroundings of the deep convective systems and some of them are entrained downwards in the cold pool with an altitude below 1000 m in the Argens valley. Thus, this dry structure is also involved in the convective-system dynamics.

5. Origin of the moisture patterns

This section aims to identify the origin of both dry and moist low-level layers over the western Mediterranean Sea involved in the MCS affecting the Var region. First, the origin of the dry air mass involved in cold-pool formation is investigated using four-day backward trajectories computed on-line with the ARP10 simulation. According to the AW2.5 backward trajectories (discussed in section 4.2), this dry air mass was located above the marine boundary layer, offshore of Catalonia (Figure 10) around 0800–0900 UTC on 14 October 2012. A total of 84 backward trajectories were computed with ARP10 for parcels within this dry air mass. They were initialized at 14 different grid points centred on 3.98°E/41.7°N and separated by roughly 0.4° and distributed over six altitudes: 1000, 1200, 1400, 1600, 1800 and 2000 m ASL. All trajectories were initialized at 0900 UTC on 14 October. For the sake of clarity, we will not show all the trajectories, but only a sample of nine representative trajectories. The trajectories are selected so as to represent all the different pathways observed, with a number of trajectories selected for each path depending on the total number of trajectories following this path. Figure 12 shows the horizontal and vertical projections of the selected backward trajectories, as well as the location of the radiosounding stations over Spain that are in the vicinity of the trajectories. For these longer-range and lower resolution backward trajectories, output with the air-parcel positions is produced every 3 h.

On 10–11 October, almost 4 days before the HPE, all trajectories originate from the north Atlantic, below 2000 m ASL for the northernmost trajectories and between 2000 m and 4000 m ASL (except from the orange trajectory) for the southernmost trajectories (Figure 12(b)). The mean water-vapour mixing ratio of the lower northernmost trajectories is about 4.7 g kg^{-1}. It increases during transport in the low levels over the ocean, probably gaining moisture from Atlantic Ocean evaporation. The moisture content is smaller for the higher southernmost trajectories (3.3–3.6 g kg^{-1}). The trajectories then reach the Iberian peninsula from the north and northeast between 0000 UTC on 11 October (southernmost trajectories) and 0300 UTC on 12 October (northernmost trajectories). They remain over land for about 2–3 days (until early 14 October), before crossing over the Western Mediterranean at an altitude above 1000 m ASL for a relatively short period (between 9 and 18 h). Over continental Spain, the lowest parcels are lifted up and dry out, while the highest trajectories continue to moisten slowly as they descend. Upon exiting Spain, all trajectories are closer to the mean water-vapour mixing ratio (5.6 g kg^{-1}). Once over the sea, the air parcels experience almost no moisture uptake (mean water-vapour mixing ratio values from 5.6 to 5.74 g kg^{-1}). The air mass involved in cold-pool formation thus results from a mixture of dry mid-level air masses (2000–3000 m ASL mainly) and low-level air masses lifted orographically over Spain, both originating from the north Atlantic.

Similarly to the dry air mass involved in cold-pool formation, the origin of the moist air feeding the precipitating systems over southeastern France is now investigated using 4 day backward trajectories computed with the ARP10 simulation. AW2.5 backward trajectories (Figure 6, discussed in section 4.1) showed that this moist air mass was located in the marine boundary layer, offshore of Catalonia around 0800–0900 UTC on 14 October 2012. A total of 90 backward trajectories were computed to sample this moist air mass. Based on AW2.5 analysis, they were initialized at 15 grid points centred on 3.88°E/41.45°N and separated by roughly 0.4° and distributed over six altitudes: 100, 300, 500, 700, 900 and 1000 m ASL. All trajectories were initialized at 0900 UTC on 14 October. As above, a sample of nine representative trajectories is chosen. Figure 13 shows the horizontal and vertical projection of the selected backward trajectories, as well as the location of the radiosounding and lidar stations over Spain and France that were in the vicinity of the trajectories. Similarly to the dry air mass backward trajectories, output with air-parcel positions is produced every 3 h.

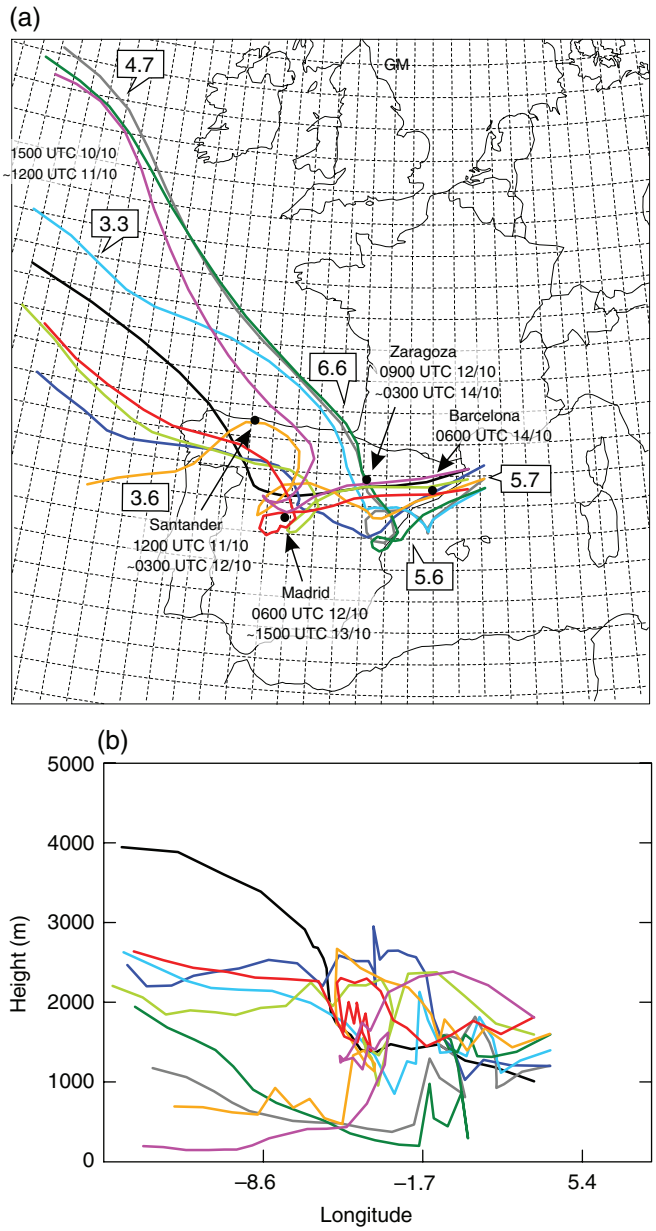

Figure 12. ARP10 backward trajectories of selected air parcels taken in the dry air flow involved in cold-pool formation: (a) horizontal projection and (b) vertical projection along the *x*-axis. The positions of the radiosounding stations over Spain are shown in (a). The approximate times at which they are overpassed by the trajectories are also indicated. The mean WVMR values (g kg^{-1}) indicated in (a) correspond to an average for all trajectories at the beginning and end of the trajectories, as well as when trajectories are crossing the northwestern and eastern coast of the Iberian Peninsula.

Almost 4 days before the HPE, all trajectories originate from the north Atlantic, mostly between 2000 and 4500 m ASL (Figure 13(b)). Their water-vapour mixing ratio is lower than 1.5 g kg^{-1}, i.e. less than the moisture content for the dry air masses, because these trajectories come from a higher altitude. They moisten slightly over the ocean as they mix with moister air at lower altitudes. Only a few trajectories (about 20%) come from altitudes below 1000 m ASL with a moisture content exceeding 4 g kg^{-1}, up to 8 g kg^{-1}. These trajectories are lifted up and dried down to about 4 g kg^{-1} before arriving over land. All trajectories reach land during the morning of 12 October, with an altitude ranging from 1000 to 3000 m ASL.

Most of the trajectories pass over France in half a day and reach the Western Mediterranean at 2100 UTC on 12 October. Over land, their moisture content increases (up to a mean water-vapour mixing ratio of 4.6 g kg^{-1}) mainly as they follow a downslope flow on the lee side of the Massif Central mountains and mix with a moister lower-level air mass. The trajectories then remain below 1000 m ASL over the sea for around 42 h before entering

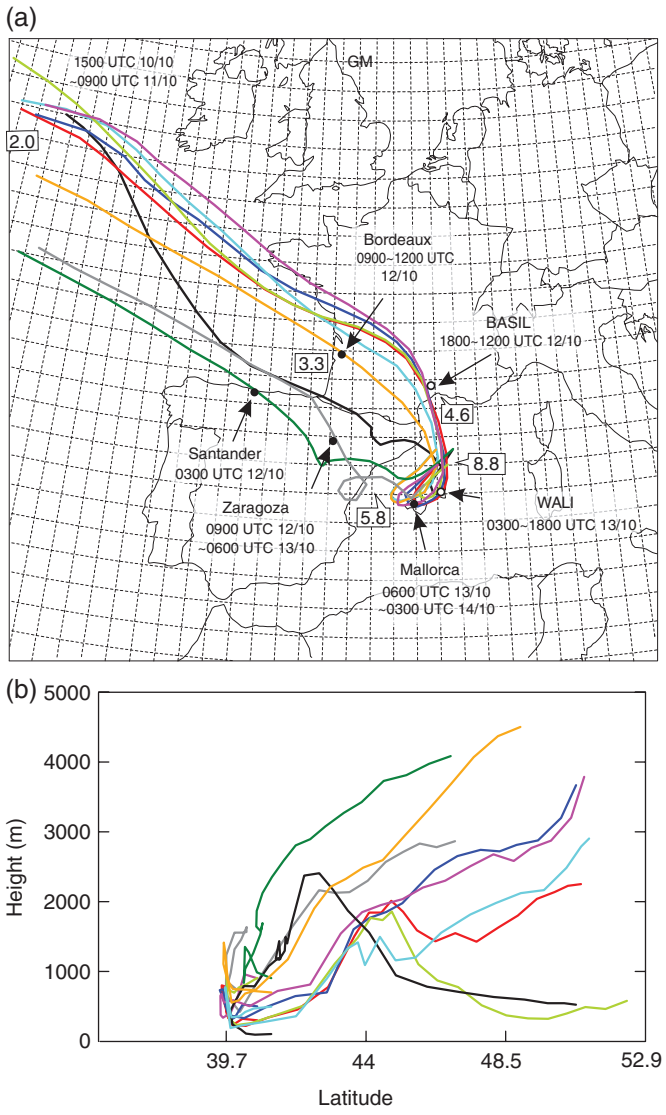

Figure 13. Same as Figure 12, but for backward trajectories of selected air parcels taken in the moist air flow feeding convection: (a) horizontal projection and (b) vertical projection along the *y*-axis. The location of the WALI and BASIL lidars are also indicated in (a), in addition to the radiosounding stations in Spain and France.

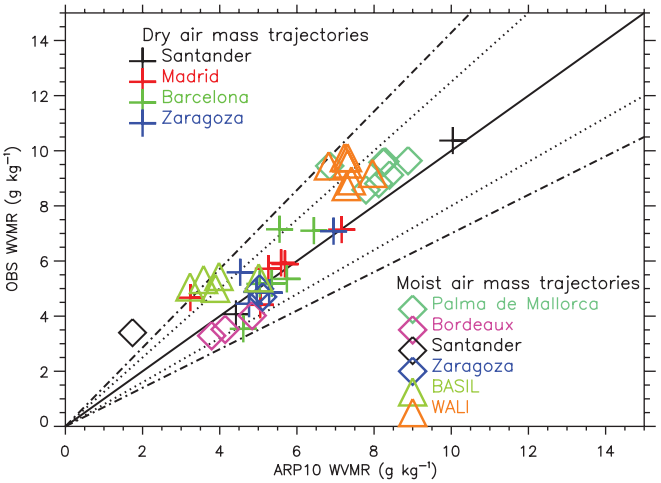

Figure 14. Scatter plot of water-vapour mixing ratios extracted from ARP10 backward trajectories against observations (radiosoundings and lidar). The crosses indicate comparisons for the trajectories originating in the cold pool over the Var region. The diamonds and triangles indicate comparisons for the trajectories of the moist air feeding convection. The solid line represents the 1:1 line, the dashed lines the 20% deviation from the 1:1 line (20% difference) and the dash–dotted lines the 30% deviation from the 1:1 line. [Colour figure can be viewed at wileyonlinelibrary.com].

the convective system. They join the northerly mistral (Jansa, 1987; Drobinski *et al.*, 2005; Di Girolamo *et al.*, 2016) and tramontane winds induced by the pressure gradient between Spain and Liguria, before heading again towards the French coast when surface pressure decreases over Spain and western France (during the night between 13 and 14 October). They experience significant moistening, with mean water-vapour mixing ratio values increasing to 8.8 g kg^{-1} over the Balearic Sea. AW2.5 backward trajectories (discussed in section 4.1) showed that the moisture uptake later on, i.e. during the end of the air-mass course over the Mediterranean, was negligible. This is consistent with the results of Rainaud *et al.* (2016), showing that, according to buoy measurements, the main increase of 2 m relative humidity before IOP13 HPE occurred over the Gulf of Lion on 12 October 2012, in the area where mistral and tramontane winds were blowing and the latent heat flux at the surface of the Mediterranean Sea was large. Hence, the evaporation of the Mediterranean appears to provide about half (4.2 g kg^{-1}) of the moisture supply to the heavy precipitation convective systems.

Some trajectories (about 20%) instead pass over Spain. They continue to moisten slowly as they descend towards lower altitudes (with about 3.4 g kg^{-1} upon entering Spain and 5.8 g kg^{-1} upon reaching the Balearic Sea). They reach the Mediterranean later (in the morning of 13 October), with a larger moisture content. Once over the sea, their moisture uptake from the sea surface is limited to about 3 g kg^{-1} (roughly 35% of the final water-vapour content). These trajectories appear similar to those obtained for dry air masses (Figure 12). Offshore of Catalonia, they are close to the marine boundary-layer top: 700 (grey line) and 900 m ASL (green line). This might evidence mixing at the top of the boundary layer between the moist boundary-layer air mass and the drier air mass above.

The different trajectories passed in the vicinity of several observation stations: four radiosounding stations for the dry trajectories of Figure 12 (Barcelona, Madrid, Santander and Zaragoza), two radiosounding sites (Bordeaux and Palma de Mallorca) as well as the two lidar stations in Candillargues and Menorca for the northernmost moist trajectories of Figure 13 and two radiosounding stations for the southernmost moist trajectories (Santander and Zaragoza). Tables A1 and A2 in the Appendix list the water-vapour mixing ratio values extracted from the 3 h output of the ARP10 backward trajectories at the closest position (in time and space) to the radiosounding and lidar stations.

Figure 14 presents a scatter plot of the water-vapour mixing ratio values extracted from backward trajectories and the observations as described in the Appendix. Such a comparison provides evidence that, for both dry and moist air masses, the water-vapour mixing ratio along the backward trajectories fo ARP10 is mostly within 20% of the radiosounding observations. The departures from lidar measurements are slightly larger but remain below 30%. The Spearman correlation coefficient is significant and equal to 0.86. Furthermore, a small bias (−0.03 g kg^{-1}) and a slope of the order of 1.12 are obtained for a linear regression. These numbers give us confidence that the water-vapour mixing ratio values extracted from the backward trajectories can be used to infer information on the moisture uptake from the sea, especially for moist air masses in the marine boundary layer feeding the MCS over the Var region. The differences between the simulated and observed water-vapour mixing ratios were not found to depend on the time difference (resulting from the fact that radiosoundings are launched at fixed times) or the distance from the trajectory to the stations (not shown).

6. Summary and outlook

During HyMeX IOP13, backbuilding heavy precipitation convective systems developed in an environment characterized by

a moist conditionally unstable marine boundary layer topped by particularly dry air masses just above. The precipitating systems and their environment were observed comprehensively by the set of instruments deployed during the first SOP of the HyMeX campaign, such as water-vapour lidars and coastal wind profilers and radiosoundings. Thanks to these observations and fine-scale numerical simulations, the moisture patterns and their relationship with the convective mechanisms involved in the development and maintenance of the backbuilding MCS were analysed.

The numerical simulation at 2.5 km horizontal resolution reproduces the heavy precipitation systems observed well, with both a realistic location and time evolution, especially for the convective line over the Var region. Convection initiation around midday and quasi-stationary maintenance during the afternoon are well simulated. The main characteristics of the marine air mass are also reproduced well with a low LFC, a low-level jet heading towards the coast and a realistic moisture content of the well-mixed layer over the sea surface and the dry air mass just above.

During the IOP13 HPE, convection is triggered and maintained by lifting over orography and over a cold pool. Strong backbuilding convective cells develop over the first foothills facing the moist and conditionally unstable low-level flow advected from the sea. Cold air formed by evaporative cooling under the precipitating cells flows down the valleys. It gradually fills up the Argens valley and spreads out over the plains, blocking the inland advection of the marine moist low-level flow. The main convective ascents and associated intense precipitation are shifted from coastal mountainsides to the coasts and over the sea, over the leading edge of the cold-air pool. In contrast to many other HPEs (Duffourg *et al.*, 2016; Scheffknecht *et al.*, 2016), no convergence is observed in the low-level marine flow feeding the precipitating systems. Surface observations confirm the simulated backbuilding mechanisms and the major impact of the cold pool on the location of the HPE.

Backward trajectories were computed to analyse the origin of the moisture structures involved in IOP13 convective mechanisms. The cold pool appears to be formed by the evaporation of part of the precipitation passing through a dry air mass located above the boundary layer. This dry air mass (water-vapour mixing between 3 g kg^{-1} and 6 g kg^{-1} for a relative humidity of 20–65%) comes from the lower half of the troposphere over the Atlantic Ocean four days before the event. Its moisture content is the result of both the advection of mid-level Atlantic air masses and the drying of low-level Atlantic air masses lifted up over Spain.

The air mass feeding the convective systems also comes from the lower half of the troposphere over the Atlantic Ocean four days before the event. The air mass mainly crosses over France and goes down in the low levels above the Mediterranean Sea along downslope flows on the lee side of the coastal mountain ranges. It remains in the lowest 1000 m above the sea for almost 48 h and moistens significantly. Most of the rise in moisture occurred due to high evaporation at the sea surface during the first hours after the air reached the Mediterranean and was located within the northerly flow of the mistral and tramontane winds. This process contributed about 50% of the total moisture supply to the HPE. This is consistent with the results of Duffourg and Ducrocq (2013). A few trajectories pass over Spain similarly to the trajectories of the dry air masses involved in the cold pool. They are probably impacted by the mixing at the top of the boundary layer. Their moisture uptake from the sea is slightly lower (about 35%), as they arrive later over the sea with a larger moisture content. A comparison with the observations available along both dry and moist trajectories (radiosoundings and lidar measurements) evidences that the simulated water-vapour mixing ratio is realistic.

The low-level moisture pattern of the environment with a moist conditionally unstable marine boundary layer topped by particularly dry air masses just above offers a plausible explanation for the formation and location over the Var coast, upstream of the Argens valley, of heavy convective precipitation during IOP13. To study further the impact of such moisture patterns on the convective mechanisms involved in the development and maintenance of heavy precipitation convective systems, a sensitivity study is currently ongoing. The characteristics of the moisture structures identified in the present article will be altered and the impact on convection will be investigated.

Acknowledgements

This work was supported by the French Agence Nationale de la Recherche (ANR) via the IODA-MED Grant ANR-11-BS56-0005 and the MUSIC Grant ANR14-CE01-014, the MISTRALS/HyMeX programme, the French space agency (CNES), the European Commission under the European Facility for Airborne Research programme of the seventh Framework Programme (Project WaLiTemp) and the Commissariat à l'Energie Atomique (CEA). Airborne data were obtained using the ATR-42 Environment Research Aircraft, operated and managed by Service des Avions Français Instrumentés pour la Recherche en Environnement (SAFIRE), which is a joint entity of CNRS, Météo-France and CNES. The SAFIRE staff are thanked for their support during the SOP1. The authors are grateful to D. Bruneau, P. Genau, C. Merlet, T. Deleporte, S. Bastin, C. Kocha, C. Lavaysse and R. Meynadier (LATMOS), as well as F. Blouzon and A. Abchiche (DT/INSU) for operating the LEANDRE 2 system aboard the ATR-42 during the HyMeX SOP1. The authors also thank F. Saïd for providing the HyMeX wind profiler dataset.

Appendix

Tables A1 and A2 list the water-vapour mixing ratio values extracted from the 3 h output of the ARP10 backward trajectories at the closest position (in time and space) to the radiosounding and lidar stations. The measured water-vapour mixing ratio values are extracted at the level of the air parcels when the backward

Table A1. Water-vapour mixing ratio (WVMR) values extracted from the 3 h output of the backward trajectories (ARP10) for selected dry air trajectories shown in Figure 12 at the closest position (in time and space) to the radiosounding measurements (RDS) of Barcelona, Zaragoza, Madrid and Santander.

Region	WVMR (g kg^{-1}) ARP10	RDS	Differences Time (h)	Distance (km)
Barcelona	5.55 (black)	7.15	0	+63.15
	6.44 (blue)	7.10	0	−4.7
	5.74 (orange)	5.35	0	−16.7
	5.35 (red)	5.19	0	−35.85
	5.04 (light green)	5.17	0	+52.3
	4.61 (magenta)	3.54	0	+92.5
Zaragoza	6.95 (grey)	7.08	+3	−46.07
	4.53 (cyan)	5.59	+6	−51.3
	4.96 (black)	4.88	0	−22.3
	5.28 (red)	4.85	0	−76.48
	4.76 (magenta)	4.45	+9	−52.34
	6.57 (green)	7.61	0	−30.15
Madrid	7.16 (orange)	7.14	−6	+106.5
	3.24 (blue)	4.67	+6	−40.7
	5.69 (light green)	5.89	+3	−66.1
	5.05 (red)	4.41	+3	−51.05
	5.59 (black)	5.93	0	−100.8
	5.26 (magenta)	5.72	+3	−69.65
Santander	10.04 (orange)	10.37	0	+146.9
	4.42 (black)	5.06	−3	+294.4

The colour indication in parentheses refers to the colour of the backward trajectories in Figure 12.

Table A2. Same as Table A1, but for selected moist air trajectories shown in Figure 13 closest (in time and space) to the radiosounding measurements (RDS) of Palma de Mallorca, Bordeaux, Zaragoza and Santander, as well as the lidar stations in Menorca (WALI) and Candillargues (BASIL).

Region	WVMR ($g\,kg^{-1}$) ARP10	RDS	Differences Time (h)	Distance (km)
Palma de Mallorca	7.79 (orange)	8.58	−6	+17.7
	8.23 (cyan)	9.58	+6	+19.21
	8.88 (magenta)	9.64	+6	−10.86
	8.40 (blue)	9.12	+3	−8.17
	8.28 (red)	9.61	−3	+11.2
	8.12 (light green)	8.81	+3	−44.89
	6.85 (grey)	9.45	+3	−17.81
Bordeaux	4.84 (cyan)	4.02	+3	+ 86.74
	4.14 (light green)	3.52	0	−117.9
	3.79 (red)	3.29	0	−110.4
Zaragoza	5.03 (grey)	4.99	+3	+63.64
	5.11 (green)	4.7	+6	−71.79
Santander	1.74 (green)	3.4	−3	+88.25
Menorca (WALI)	7.41 (orange)	8.91	0	−15.69
	6.82 (cyan)	9.45	0	+37.44
	7.28 (magenta)	8.7	0	−14.03
	7.23 (light green)	9.75	0	+45.38
	7.31 (red)	9.75	0	−49.87
	7.31 (blue)	9.52	0	−47.35
	7.96 (black)	9.18	0	−47.44
Candillargues (BASIL)	3.58 (blue)	5.33	0	−52.45
	3.23 (magenta)	5.06	0	+38
	3.98 (red)	5.44	0	+59.66
	5.01 (cyan)	5.39	0	+87.8
	3.89 (light green)	5.01	0	+69.75

trajectories are at their closest position to the observation station. The time difference and horizontal distance between the closest encounters are also given. The sign convention associated with time and distance is as follows: the 'minus' sign refers to parcels approaching the station, while the 'plus' sign refers to parcels moving away from the station.

References

Barthlott C, Davolio S. 2016. Mechanisms initiating heavy precipitation over Italy during HyMeX special observation period 1: A numerical case study using two mesoscale models. *Q. J. R. Meteorol. Soc.* **142**: 238–258. https://doi.org/10.1002/qj.2630.

Barthlott C, Adler B, Kalthoff N, Handwerker J, Kohler M, Wieser A. 2016. The role of Corsica in initiating nocturnal offshore convection. *Q. J. R. Meteorol. Soc.* **142**: 222–237. https://doi.org/10.1002/qj.2415.

Bougeault P, Lacarrère P. 1989. Parameterization of orography-induced turbulence in a meso-beta-scale model. *Mon. Weather Rev.* **117**: 1872–1890.

Bresson E, Ducrocq V, Nuissier O, Ricard D, de Saint-Aubin C. 2012. Idealized numerical study of Southern France heavy precipitating events: Identification of favouring ingredients. *Q. J. R. Meteorol. Soc.* **134**: 131–145. https://doi.org/10.1002/qj.199.

Bruneau D, Quaglia P, Flamant C, Meissonnier M, Pelon J. 2001. Airborne lidar LEANDRE II for water-vapor profiling in the troposphere. I. System description. *Appl. Opt.* **40**: 3450–3461. https://doi.org/10.1364/AO.40.003450.

Buzzi A, Davolio S, Malguzzi P, Drofa O, Mastrangelo D. 2014. Heavy rainfall episodes over Liguria of autumn 2011: Numerical forecasting experiments. *Nat. Hazards Earth Syst. Sci.* **14**: 1325–1340. https://doi.org/10.5194/nhess-14-1325-2014.

Caniaux G, Redelsperger JL, Lafore JP. 1994. A numerical study of the stratiform region of a fast-moving squall line. *J. Atmos. Sci.* **51**: 2046–2074.

Chazette P, Marnas F, Totems J. 2014. The mobile water vapor Aerosol Raman LIdar and its implication in the frame of the HyMeX and ChArMEx programs: Application to a dust transport process. *Atmos. Meas. Tech.* **7**: 1629–1647. https://doi.org/10.5194/amt-7-1629-2014.

Collela P, Woodward PR. 1984. The piecewise parabolic method (PPM) for gas dynamical simulations. *J. Comput. Phys.* **54**: 174–201. https://doi.org/10.1016/0021-9991(84)90143-8.

Courtier P, Freydier C, Geleyn J-F, Rabier F, Rochas M. 1991. The ARPEGE project at Météo-France. In *Proceedings of ECMWF Seminar on Numerical Methods in Atmospheric Models*, **II**, 9–13 September 1991. 193–231. Shinfield Park Reading, UK.

Cuxart J, Bougeault P, Redelsperger JL. 2000. A turbulence scheme allowing for mesoscale and large-eddy simulations. *Q. J. R. Meteorol. Soc.* **126**: 1–30. https://doi.org/10.1002/qj.49712656202.

Davolio S, Volont A, Manzato A, Pucillo A, Cicogna A, Ferrario ME. 2016. Mechanisms producing different precipitation patterns over north-eastern Italy: Insights from HyMeX-SOP1 and previous events. *Q. J. R. Meteorol. Soc.* **142**: 188–205. https://doi.org/10.1002/qj.2731.

Di Girolamo P, Summa D, Ferretti R. 2009. Multiparameter Raman Lidar measurements for the characterization of a dry stratospheric intrusion event. *J. Atmos. Oceanic Technol.* **26**: 1742–1762. https://doi.org/10.1175/2009JTECHA1253.1.

Di Girolamo P, Flamant C, Cacciani M, Richard E, Ducrocq V, Summa D, Stelitano D, Fourrié N, Saïd F. 2016. Observation of low-level wind reversals in the Gulf of Lion area and their impact on the water vapour variability. *Q. J. R. Meteorol. Soc.* **142**: 153–172. https://doi.org/10.1002/qj.2767.

Doerenbecher A, Basdevant C, Bernard F, Cocquerez P, Verdier N, Durand P. 2013. Boundary layer pressurized balloons deployed in the Mediterranean. In *Proceedings of the 21st ESA Symposium on European Rocket and Balloons Programmes and Related Research*, 9–13 June 2013. Thun, Switzerland, (ESA SP-721, due November 2013). 99–106. ESA Publications division: ESTEC, Noordwijk, Netherlands.

Drobinski P, Bastin S, Guénard V, Caccia JL, Dabas AM, Delville P, Protat A, Reitebuch O, Werner C. 2005. Summer Mistral at the exit of the Rhône Valley. *Q. J. R. Meteorol. Soc.* **131**: 353–375. https://doi.org/10.1256/qj.04.63.

Ducrocq V, Nuissier O, Ricard D. 2008. A numerical study of three catastrophic precipitating events over Southern France. Part II: Mesoscale trigerring and stationarity factors. *Q. J. R. Meteorol. Soc.* **134**: 131–145.

Ducrocq V, Braud I, Davolio S, Ferretti R, Flamant C, Jansa A, Kalthoff N, Richard E, Taupier-Letage I, Ayral PA, Belamari S, Berne A, Borga M, Boudevillain B, Bock O, Boichard JL, Bouin MN, Bousquet O, Bouvier C, Chiggiato J, Cimini D, Corsmeier U, Coppola L, Cocquerez P, Defer E, Delanoë J, Di Girolamo P, Doerenbecher A, Drobinski P, Dufournet Y, Fourrié N, Gourley JJ, Labatut L, Lambert D, Coz JL, Marzano FS, Molinié G, Montani A, Nord G, Nuret M, Ramage K, Rison W, Roussot O, Saïd F, Schwarzenboeck A, Testor P, Baelen JV, Vincendon B, Aran M, Tamayo J. 2014. HyMeX-SOP1: The field campaign dedicated to heavy precipitation and flash flooding in the Northwestern Mediterranean. *Bull. Am. Meteorol. Soc.* **95**: 1083–1100. https://doi.org/10.1175/BAMS-D-12-00244.1.

Duffourg F, Ducrocq V. 2013. Assessment of the water supply to Mediterranean heavy precipitation: A method based on finely design water budget. *Atmos. Sci. Lett.* **14**: 133–138. https://doi.org/10.1002/asl2.429.

Duffourg F, Nuissier O, Ducrocq V, Flamant C, Chazette P, Delanoë J, Doerenbecher A, Fourrié N, Di Girolamo P, Lac C, Legain D, Martinet M, Saïd F, Bock O. 2016. Offshore deep convection initiation and maintenance during the HyMeX IOP 16a heavy precipitation event. *Q. J. R. Meteorol. Soc.* **142**: 259–274. https://doi.org/10.1002/qj.2725.

Fourrié N, Bresson E, Nuret M, Jany C, Brousseau P, Doerenbecher A, Kreitz M, Nuissier O, Sevault E, Bénichou H, Amodei M, Pouponneau F. 2015. AROME-WMED, a real-time mesoscale model designed for the HyMeX Special Observation Periods. *Geosci. Model Dev.* **8**: 1801–1856. https://doi.org/10.5194/gmdd-8-1801-2015.

Gal-Chen T, Somerville RCJ. 1975. On the use of a coordinate transformation for the solution of the Navier–Stokes equations. *J. Comput. Phys.* **17**: 209–228. https://doi.org/10.1016/0021-9991(75)90037-6.

Gheusi F, Stein J. 2002. Lagrangian description of airflows using Eulerian passive tracers. *Q. J. R. Meteorol. Soc.* **128**: 337–360. https://doi.org/10.1256/00359000260498914.

Jansa A. 1987. Distribution of the mistral: A satellite observation. *Atmos. Phys.* **36**: 201–214. https://doi.org/10.1007/BF01045149.

Kain JS, Fritsch JM. 1993. Convective parameterization for mesoscale models: The Kain–Fritsch scheme. In *The representation of cumulus convection in numerical models*, Emanuel KA, Raymond DJ. (eds.): Meteorological Monograph **46**: 165–170. American Meteorological Society: Boston, MA, USA.

Lafore JP, Stein J, Asencio N, Bougeault P, Ducrocq V, Duron J, Fischer C, Hreil P, Mascart P, Masson V, Pinty JP, Redelsperger JL, Richard E, Vil-Guerau de Arellano J. 1998. The Meso-NH atmospheric simulation system. Part I: Adiabatic formulation and control simulations. *Ann. Geophys.* **16**: 90–109. https://doi.org/10.1007/s00585-997-0090-6.

Lee KO, Flamant C, Ducrocq V, Duffourg F, Fourrié N, Davolio S. 2016. Convective initiation and maintenance processes of two back-building mesoscale convective systems leading to heavy precipitation events in southern Italy during HyMeX IOP 13. *Q. J. R. Meteorol. Soc.* **142**: 2623–2635. https://doi.org/10.1002/qj.2851.

Lee KO, Flamant C, Ducrocq V, Duffourg F, Fourrié N, Delanoe J, Bech J. 2017. Initiation and development of a mesoscale convective system in the Ebro River Valley and related heavy precipitation over north-eastern Spain during HyMeX IOP 15a. *Q. J. R. Meteorol. Soc.* **143**: 942–956.

Llasat MC, Llasat-Botija M, Petrucci O, Pasqua AA, Rosselló J, Vinet F, Boissier L. 2013. Towards a database on societal impact of Mediterranean floods

within the framework of the HYMEX project. *Nat. Hazards Earth Syst. Sci.* **13**: 1337–1350. https://doi.org/10.5194/nhess-13-1337-2013.

Martínez C, Campins J, Jansà A, Genovés A. 2008. Heavy rain events in the Western Mediterranean: An atmospheric pattern classification. *Adv. Sci. Res.* **2**: 61–64. https://doi.org/10.5194/asr-2-61-2008.

Masson V, Le Moigne P, Martin E, Faroux S, Alias A, Alkama R, Belamari S, Barbu A, Boone A, Bouyssel F, Brousseau P, Brun E, Calvet JC, Carrer D, Decharme B, Delire C, Donier S, Essaouini K, Gibelin AL, Giordani H, Habets F, Jidane M, Kerdraon G, Kourzeneva E, Lafaysse M, Lafont S, Lebeaupin Brossier C, Lemonsu A, Mahfouf JF, Marguinaud P, Mokhtari M, Morin S, Pigeon G, Salgado R, Seity Y, Taillefer F, Tanguy G, Tulet P, Vincendon B, Vionnet V, Voldoire A. 2013. The SURFEXv7.2 land and ocean surface platform for coupled or offline simulation of earth surface variables and fluxes. *Geosci. Model Dev.* **6**: 929–960. https://doi.org/10.5194/gmd-6-929-2013.

Miglietta M, Rotunno R. 2010. Numerical simulations of low-CAPE flows over a mountain ridge. *J. Atmos. Sci.* **67**: 2391–2401. https://doi.org/10.1175/2010JAS3378.1.

Mlawer EJ, Taubman SJ, Brown PD, Iacono MJ, Clough SA. 1997. Radiative transfer for inhomogeneous atmospheres: RRTM, a validated correlated-k model for the longwave. *J. Geophys. Res.* **102**: 16 663–16 682. https://doi.org/10.1029/97JD00237.

Nuissier O, Ducrocq V, Ricard D. 2008. A numerical study of three catastrophic precipitating events over Southern France. Part I: Numerical framework and synoptic ingredients. *Q. J. R. Meteorol. Soc.* **134**: 111–130. https://doi.org/10.1002/qj.200.

Nuissier O, Joly B, Joly A, Ducrocq V, Arbogast P. 2011. A statistical downscaling to identify the large-scale circulation patterns associated with heavy precipitation events over Southern France. *Q. J. R. Meteorol. Soc.* **137**: 1812–1827. https://doi.org/10.1002/qj.866.

Pergaud J, Masson V, Malardel S, Couvreux F. 2009. A parameterization of dry thermals and shallow cumuli for mesoscale numerical weather prediction. *Boundary Layer Meteorol.* **132**: 83–106. https://doi.org/10.1007/s10546-009-9388-0.

Pinty JP, Jabouille P. 1998. A mixed-phased cloud parametrization for use in a mesoscale non-hydrostatic model: Simulations of a squall line and of orographic precipitation. In *Proceedings of the Conference on Cloud Physics*, 17–21 August 1998. Everett, WA. American Meteorological Society: Boston, MA, 217–220.

Rainaud R, Lebeaupin-Brossier C, Ducrocq V, Giordani H, Nuret M, Fourrié N, Bouin MN, Taupier-Letage I, Legain D. 2016. Characterization of airsea exchanges over the Western Mediterranean Sea during HyMeX SOP1 using the AROME-WMED model. *Q. J. R. Meteorol. Soc.* **142**: 173–187. https://doi.org/10.1002/qj.2480.

Ricard D, Ducrocq V, Auger L. 2012. A climatology of the mesoscale environment associated with heavily precipitating events over a Northwestern Mediterranean area. *J. Appl. Meteorol. Climatol.* **51**: 468–488. https://doi.org/10.1175/JAMC-D-11-017.1.

Romero R, Doswell CA III, Ramis C. 2000. Mesoscale numerical study of two cases of long-lived quasi-stationary convective systems over Eastern Spain. *Mon. Weather Rev.* **128**: 3731–3751.

Rudari R, Entekhabi D, Roth G. 2004. Terrain and multiple-scale interactions as factors in generating extreme precipitation events. *J. Hydrometeorol.* **5**: 390–404.

Saïd F, Campistron B, Delbarre H, Canut G, Doerenbecher A, Durand P, Fourrié N, Lambert D, Legain D. 2016. Offshore winds obtained from a network of wind-profiler radars during HyMeX. *Q. J. R. Meteorol. Soc.* **142**: 23–42. https://doi.org/10.1002/qj.2749.

Schär C, Wernli H. 1993. Structure and evolution of an isolated semi-geostrophic cyclone. *Q. J. R. Meteorol. Soc.* **119**: 57–90. https://doi.org/10.1002/qj.49711950904.

Scheffknecht P, Richard E, Lambert D. 2016. A highly localized high-precipitation event over Corsica. *Q. J. R. Meteorol. Soc.* **142**: 206–221. https://doi.org/10.1002/qj.2795.

Schumacher RS, Johnson RH. 2005. Organization and environmental properties of extreme-rain-producing mesoscale convective systems. *Mon. Weather Rev.* **133**: 961–976. https://doi.org/10.1175/MWR2899.1.

Seity Y, Brousseau P, Malardel S, Hello G, Bernard P, Bouttier F, Lac C, Masson V. 2011. The AROME-France convective-scale operational model. *Mon. Weather Rev.* **139**: 976–991. https://doi.org/10.1175/2010MWR3425.1.

Shu CW, Osher S. 1988. Efficient implementation of essentially non-oscillatory shock-capturing schemes. *J. Comput. Phys.* **77**: 439–471.

